

Resolving phase transition properties of dense matter through tidal-excited g-mode from inspiralling neutron stars

Zhiqiang Miao¹, Enping Zhou² and Ang Li¹

¹*Department of Astronomy, Xiamen University, Xiamen, Fujian 361005, China; liang@xmu.edu.cn*

²*Department of Astronomy, School of Physics, Huazhong University of Science and Technology, Wuhan, 430074, China*

The investigation of the phase state of dense matter is hindered by complications of first-principle nonperturbative quantum chromodynamics. By performing the first consistent general-relativistic calculations of tidal-excited g-mode of neutron stars with a first-order strong interaction phase transition in the high-density core, we demonstrate that gravitational wave signal during binary neutron star inspiral probes their innermost hadron-quark transition and provides potent constraints from present and future gravitational-wave detectors.

Introduction. – Despite decades of exploration, the phase state of cold, dense matter is still a fundamental problem that remains unresolved. This problem pertains to low-energy nonperturbative quantum chromodynamics (QCD) [1] and is one of the key scientific goals in current and anticipated relativistic heavy-ion collision experiments [2]. It is widely believed that this type of matter exists in the core of neutron stars (NSs). The equation of state (EoS) of dense stellar matter has drawn much attention in the era of gravitational wave (GW) astronomy. This is because the observations of GW170817 led to the first measurement of NS tidal deformability [3], which offered valuable insight into the phase state of dense matter [4].

The tidal deformability accounts for the quadrupole deformations of inspiralling NSs, which are induced by the tidal force from each other, when the quasi-equilibrium approximation can be utilized (i.e., the tidal field changes slowly). While in the late stage of the inspiral phase, once the binary's orbital frequency approaches the frequency of a particular normal mode of NSs, a resonance can occur. This resonance will transfer the orbital energy to the stellar oscillation via a mechanism referred to as the dynamical tide. This event will accelerate the orbital decay and result in a phase shift in the GW waveform, which will provide insights into the NS inner structure with the help of GW detection from inspiralling NSs.

Previous studies have focused on the interfacial (i) modes, which are excited at the interface between the solid crust and fluid core [5–7]. These modes typically have frequencies of ~ 100 Hz and contribute $\sim \mathcal{O}(0.1)$ phase shifts during resonance, making them promising candidates for detection using Advanced LIGO (aLIGO) [8] and 3rd generation GW detectors such as Einstein Telescope (ET) [9] and Cosmic Explorer (CE) [10]. Attempts have also been made to infer NS EoS through tide-induced f-modes and g-modes, which arise from the composition gradients within the NS's interior. Studies (see e.g., Refs. [11–16]) have shown that f-modes are challenging to excite due to their high resonant frequencies, whereas g-modes demonstrate negligible phase shifts because their couplings to tidal fields are meager.

In this Letter, we investigate a unique type of g-modes, known as discontinuity g-modes, which are expected to occur in NSs that possibly have a strong phase transition in their high-density inner cores. Our study showcases how discon-

tinuity g-modes' dynamical tide can be leveraged to probe the dense matter's phase transition properties using the data obtained from GW170817, along with possible observations from the next-generation GW detectors.

G-modes of hybrid stars. – The existence of a quark core inside NSs (also called hybrid stars) has been discussed with Newtonian formulations of perturbations and tidal couplings, focusing on the i-mode at the interface of a crystalline quark core and a fluid hadronic envelope [17]. With the solid quark core condition relaxed, we here employ a full general relativistic (GR) formalism as follows: 1) Constructing the background hybrid stars in hydrostatic equilibrium using Einstein's field equations, specifically the Tolman-Oppenheimer-Volkoff equations, and 2) Computing their discontinuity g-modes by solving the linear pulsation equations in general relativity [18, 19]. This study focuses solely on the $l = 2$ g-modes, as they have the strongest coupling to the tidal gravitational field. We use the generic constant-speed-of-sound (CSS) parameterization [20] to construct the sharp first-order hadron-quark phase transition and model the quark matter in the high-density cores of NSs. Previous studies have thoroughly discussed the weak density dependence of the speed of sound in quark matter (see e.g., Refs. [20, 21]). This allows us to determine the equation of state (EoS) from the start of the phase transition up to the maximum central density of the star by using three phase-transition parameters: the transition density ε_t , the transition strength $\Delta\varepsilon$ and the speed of sound in quark matter c_s . The QMF [22] and NL3 $\omega\rho$ [23] models are employed to describe the fiducial soft and stiff hadronic matter, respectively, while maintaining consistency with laboratory nuclear experiments.

It is worth noting that since the discontinuity g-modes are a result of the discontinuity in the density profile of the star, we expect the frequency of these modes to depend on both the transition strength and the transition density. Based on our calculations, we observe that the g-mode frequency typically falls within the range of 100 Hz to 1500 Hz, which is strongly dependent on the transition strength. The transition strength varies between ~ 5 MeV/fm³ and ~ 300 MeV/fm³. Our study also indicates that the speed of sound (c_s) has a subdominant effect on mode frequency. Specifically, the difference in mode frequency between the $c_s = 1/\sqrt{3}$ case (corresponding to the conformal limit) and the $c_s = 1$ case (corresponding to

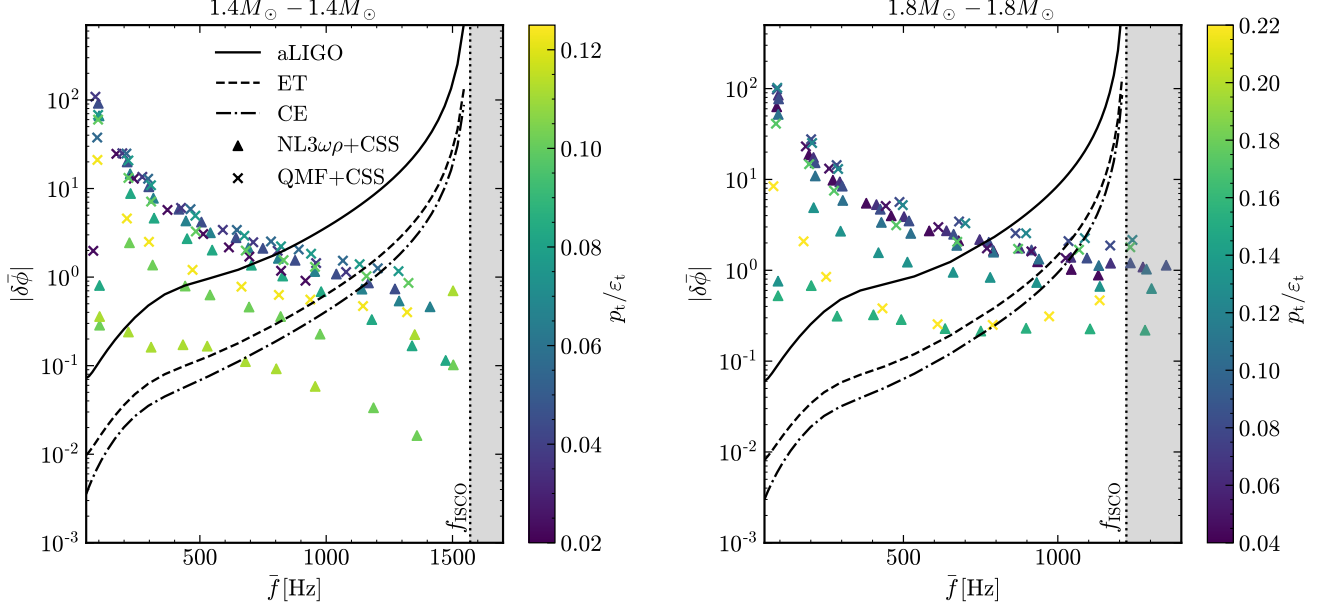


FIG. 1. Total phase shift $|\delta\bar{\phi}|$ and resonant frequency \bar{f} for a $1.4 M_{\odot} - 1.4 M_{\odot}$ system (left panel) and a $1.8 M_{\odot} - 1.8 M_{\odot}$ system (right panel), depending on the transition densities (represented by p_t/ε_t). $f_{\text{ISCO}} \simeq 4400 \text{ Hz}/(M + M')$ denotes the GW frequency corresponding to the innermost stable circular orbit, at which we assume the signal of inspiral phase shut off [24]. Also plotted are the detectability thresholds of aLIGO, ET and CE, which are calculated from their designed sensitivities by assuming the system is located at $D_L = 100 \text{ Mpc}$.

the casual limit) is found to be less than $\sim 10\%$. Thus, for the purpose of our analysis, we solely focus on extremely stiff quark matter with a speed of sound $c_s = 1$.

Tidal coupling and waveform correction.—Throughout the inspiral process, the binary's individual components will be subject to external tidal forces from their respective companions. Upon the tidal driving frequency nearing the g-mode frequency of the NSs, it becomes possible to trigger internal stellar oscillations through resonance, ultimately causing a phase shift in the GW waveform. The phase shift resulting from mode resonance in a single star is represented as [13]:

$$\delta\phi \simeq -0.12 \left(\frac{Q}{0.01}\right)^2 \left(\frac{600 \text{ Hz}}{f}\right)^2 \left(\frac{2q}{1+q}\right) M_{1.4}^{-4} R_{12}^2, \quad (1)$$

where $q = M'/M$ with M' representing the companion star mass. Q is the tidal overlap integral between the $l = 2$ g-mode and the tidal field, and here we take its relativistic form [25],

$$Q = \frac{1}{MR^2} \int \sqrt{-g} e^{-2\Phi} d^3x (p + \varepsilon) \xi^{*\mu} \nabla_{\mu} (r^2 Y_{2m}), \quad (2)$$

to account for the GR treatment of the perturbation. Here, g represents the determinant of the metric of the background spacetime and $e^{2\Phi} = g_{tt}$ is the (t, t) component of the metric. $\xi^{\mu} = (0, r e^{-\lambda} W Y_{2m}, V \partial_{\theta} Y_{2m}, V \sin^{-2} \partial_{\phi} Y_{2m})$ is the Lagrangian displacement of the eigenmode with the normalization $\int \sqrt{-g} d^3x e^{-2\Phi} (p + \varepsilon) \xi^{*\mu} \xi_{\mu} = MR^2$. Y_{2m} is the $l = 2$ spherical harmonic. The transition density and tran-

sition strength affect the tidal overlap integral and its typical value remains at $\sim \mathcal{O}(0.01)$.

The total phase correction for a binary NS waveform $h(f) = \mathcal{A} e^{i\Psi(f)}$, which takes into account the mode resonances of both components, is expressed as [6, 26]:

$$\begin{aligned} \Delta\Psi(f) &= -\sum_i \delta\phi_i \left(1 - \frac{f}{f_i}\right) \Theta(f - f_i) \\ &\approx -\delta\bar{\phi} \left(1 - \frac{f}{\bar{f}}\right) \Theta(f - \bar{f}), \end{aligned} \quad (3)$$

where f_i is the g-mode frequency of the i -th star and $\delta\bar{\phi}_i$ represents the corresponding phase shift due to resonance. Here, $\Theta(\cdot)$ is the Heaviside step function. The second line of Eq. (3) introduces the total phase shift $\delta\bar{\phi} = \sum_i \delta\phi_i$ and the resonant frequency $\bar{f} = \delta\bar{\phi} / \sum_i (\delta\phi_i / f_i)$ to reduce the number of parameters [6]. For simplicity, $|\delta\bar{\phi}|$ will be used as the waveform parameter from here on.

Detectability.—Fig. 1 displays the total phase shift $|\delta\bar{\phi}|$ against the resonant frequency \bar{f} for two equal-mass binary systems, along with the detection thresholds of aLIGO and 3rd generation detectors. These thresholds are computed using a Fisher matrix method [24] and are based on the designed sensitivities [27] assuming that the binary systems are located at $D_L = 100 \text{ Mpc}$. Generally, $|\delta\bar{\phi}|$ decreases with the increase of \bar{f} since $\delta\phi \propto f^{-2}$. For a significant number of hybrid star models, the total phase shifts are greater than the detectability threshold of 3rd generation detectors. It is worth

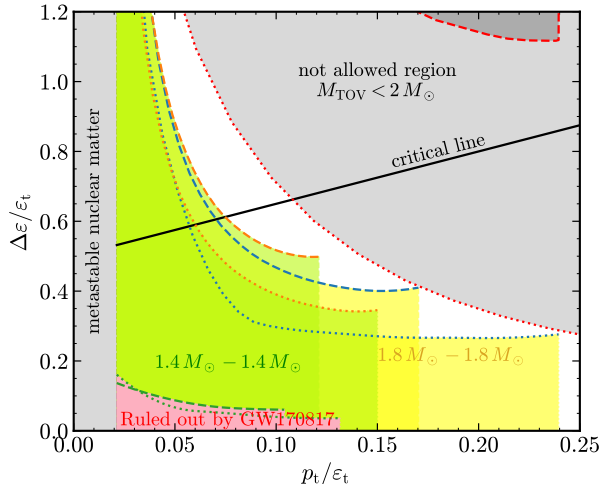


FIG. 2. Detectable regions of phase transition parameters for a $1.4 M_\odot - 1.4 M_\odot$ system (green) and a $1.8 M_\odot - 1.8 M_\odot$ system (yellow) on the 3rd generation detectors. The red region depicts the parameter space ruled out by the mode resonance analysis of GW170817 at 95% confidence level, and the grey regions represent the portions eliminated by the maximum mass of observed pulsars. The results of QMF+CSS and NL3 $\omega\rho$ +CSS are represented by dotted and dashed lines, respectively. The critical line corresponds to $\Delta\varepsilon/\varepsilon_t = 1/2 + 3p_t/2\varepsilon_t$, dividing the parameter space into two parts. Below the critical line, there is a hybrid star branch connected to the hadronic branch, while above the critical line, there is no connected hybrid star branch [20].

noting that there is a threshold frequency f_{th} , which is independent of the hadronic EoS. Binaries with $\bar{f} \lesssim f_{\text{th}}$ may be detectable by 3rd generation detectors, while those with $\bar{f} \gtrsim f_{\text{th}}$ may not be detectable. For a $1.4 M_\odot - 1.4 M_\odot$ system, $f_{\text{th}} \simeq 1200$ Hz, while for a $1.8 M_\odot - 1.8 M_\odot$ system, $f_{\text{th}} \simeq 1050$ Hz. These threshold frequencies lead to constraints on the phase transition parameters, which are illustrated in the shaded regions (green for $1.4 M_\odot - 1.4 M_\odot$ system and yellow for $1.8 M_\odot - 1.8 M_\odot$ system) in Fig. 2. It is evident that the detection of a signal of mode resonance provides a new opportunity to probe the properties of the hadron-quark phase transition, which can serve as a complementary constraint to other observations, such as the $\sim 2 M_\odot$ maximum mass constraint from the most massive pulsars (grey regions in Fig. 2). In addition, we have derived two helpful approximations for the mode frequency and tidal overlap integral, which are outlined in the Supplemental Material. These approximations can aid in determining phase transition properties once mode resonance signatures are detected in the future. Even if no mode resonance signal is detected, the upper limit of the phase shift can further rule out a considerable parameter space.

GW170817 constraints.—We now utilize the available GW170817 data and conduct a search for mode resonance signals, utilizing waveform correction as outlined in Eq. (3).

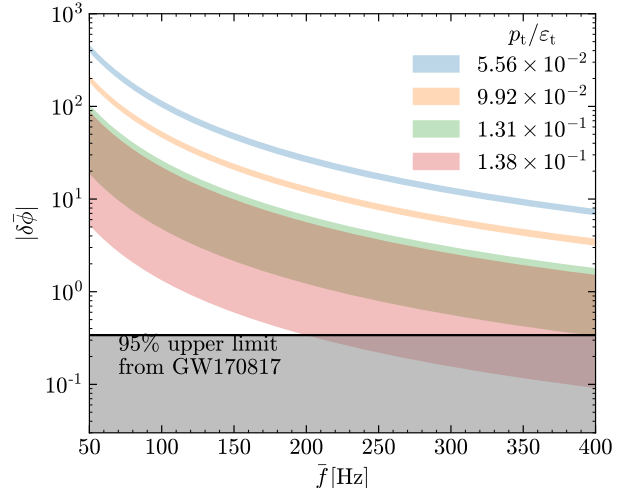


FIG. 3. Constraints on phase transition densities (represented by p_t/ε_t) with GW170817 data for QMF+CSS models. The shaded regions depict calculations for a GW170817-like system with chirp mass $\mathcal{M} = 1.186 M_\odot$ and mass ratio $q = 0.7-1$. The horizontal line denotes the 95% upper limit of $|\delta\bar{\phi}| < 0.34$ obtained with a low-frequency prior.

This is similar to a previous search conducted in Ref. [6] for signals in the frequency range of [30, 300] Hz. We employ a Bayesian parameter estimation approach, following the data analysis framework presented in Ref. [28]. Our analysis utilizes PYMULTINEST [29] implemented in BILBY [30], which enabled the simultaneous acquisition of the posterior distribution of parameters and the model evidence \mathcal{Z} . By denoting \mathcal{H}_1 as the hypothesis with mode resonance and \mathcal{H}_0 as the one without, we are able to compute the Bayes factor from the evidence, $\mathcal{B}_0^1 = \mathcal{Z}_1/\mathcal{Z}_0$. We adopt two distinct sets of prior distributions for $|\delta\bar{\phi}|$ and \bar{f} in hypothesis \mathcal{H}_1 . The first is a low-frequency prior characterized by $|\delta\bar{\phi}| \sim \text{LogU}[10^{-4}, 10^2]$ and $\bar{f} \sim \text{U}[50, 400]$ Hz. The second is a high-frequency prior characterized by $|\delta\bar{\phi}| \sim \text{LogU}[10^{-4}, 10^2]$ and $\bar{f} \sim \text{U}[50, 1600]$ Hz. Here, U denotes a uniform distribution, while LogU represents a logarithmic uniform distribution. We obtain Bayes factors $\mathcal{B}_0^1 = 0.65$ and $\mathcal{B}_0^1 = 0.72$ for the low-frequency and high-frequency priors, respectively. Since these Bayes factors are close to unity, it implies that the two hypotheses are consistent with each other, regardless of the choice of prior [31]. We further determine the 95% upper limit of the total phase shift to be $|\delta\bar{\phi}| < 0.34$ for the low-frequency prior case. This upper limit can be utilized to set constraints on the phase transition parameters. In Fig. 3, we present the total phase shift and the resonant frequency for a GW170817-like system with a chirp mass of $\mathcal{M} = 1.186 M_\odot$ and a mass ratio range of $q = 0.7-1$. The 95% upper limit of $|\delta\bar{\phi}|$ indicates that hybrid star models with $\bar{f} \lesssim 400$ Hz and $p_t/\varepsilon_t \lesssim 0.13$ are strongly disfavored by GW 170817 observations. By converting these constraints on \bar{f} to phase transition properties, we conclusively rule out the possibility of a

weak phase transition ($\Delta\varepsilon/\varepsilon_t \lesssim 0.1$) occurring at low densities ($\rho_t/\varepsilon_t \lesssim 0.13$) with a confidence level of 95%. We have depicted this region as the red region in Fig. 2. Our conclusion is in agreement with our previous findings based on static tidal deformability constraints from GW170817 [32] and the study of proton and lambda production during relativistic heavy-ion collisions at several GeV/nucleon incident beam energies [33].

Discussion. – The investigation of phase transitions in QCD matter is a central area of interest in physics and has relevance for a range of open problems, such as early Universe [34, 35], core-collapse supernovae [36], cosmological gamma-ray bursts [37], as well as the nonperturbative properties of QCD itself [38]. We propose to probe the phase transition properties possible in dense NS matter through the tidal resonant excitation of g-modes. Our analysis demonstrates that the tidal excitation of g-modes from inspiralling neutron stars can induce significant phase shifts in the gravitational waveform, on the order of $\sim \mathcal{O}(0.1) - \mathcal{O}(1)$. These shifts are detectable by both aLIGO and 3rd generation detectors. Notably, these low-frequency signatures complement previous efforts to identify first-order phase transitions using high-frequency post-merger gravitational waves [39], expanding the range of density regimes that can be probed for potential phase transitions. We propose two analytical formulas to clarify the relationship between the phase shift in the gravitational waveform and the properties of the phase transition. These formulas will be useful for future efforts to directly estimate phase transition parameters using GW data. Our analysis indicates that the estimation errors are moderate, with a maximum of approximately 15% for the mode frequencies and 25% for the tidal overlap integrals (as detailed in the Supplemental Material). This leads to a possible underestimation or overestimation of the phase shift by a factor of no more than 2-3.

To calculate the correction to the gravitational waveform induced by the g-mode resonance, we use the form presented in Eq. (3). However, it is important to note that this form is derived under the assumption that the energy transfer of the resonance is instantaneous [26]. Therefore, it is only valid when the duration of the resonance, $t_{\text{res}} \simeq 0.009s (\mathcal{M}/1.2 M_\odot)^{-5/6} (f/600 \text{ Hz})^{-11/6}$, is much shorter than the orbital decay time-scale, $t_D \simeq 0.08s (\mathcal{M}/1.2 M_\odot)^{-5/3} (f/600 \text{ Hz})^{-8/3}$ [13]. For resonant frequencies that are very high (e.g., $\gtrsim 1000$ Hz), the waveform correction $\Delta\Psi(f)$ should be modified to account for the continuous process of energy transfer during the resonance. It is also important to consider the relativistic corrections to the Newtonian orbit as the binary approaches closer, especially for high resonant frequencies. These improvements will be the subject of future work.

In addition, it is crucial to identify the physical origin of the mode resonance signature once it is detected. This is because there could be other possible origins apart from the resonant excitation of hybrid star g-modes. As suggested by Ref. [6], other processes such as tidal-p-g coupling [40] or

those in modified gravity [41, 42] predict different corrections on the waveform. Therefore, one could perform a Bayesian model selection to compare these different origins. On the other hand, crust melting can produce a $\Delta\Psi(f)$ similar to the resonant excitation of g-modes considered here. However, the resonant frequencies associated with the crust melting are typically ~ 100 Hz, whereas hybrid star g-modes have frequencies ranging from ~ 400 Hz to ~ 1200 Hz. Our Fisher analysis shows that the resonant frequencies can be measured with a precision of $\lesssim 10\%$ using 3rd generation detectors (see Supplemental Material). This precision would enable us to discriminate between the g-mode resonance considered here and the crust melting process by comparing their frequencies.

We thank Dong Lai, Lap-Ming Lin, Yuxin Liu, Yong Gao and Zhenyu Zhu for their helpful comments. The work is supported by the National SKA Program of China (No. 2020SKA0120300) and the National Natural Science Foundation of China (grant Nos. 12273028, 12203017 and 11873040). This research has made use of data and software obtained from the Gravitational Wave Open Science Center <https://www.gw-open-science.org>, a service of LIGO Laboratory, the LIGO Scientific Collaboration and the Virgo Collaboration. LIGO is funded by the U.S. National Science Foundation. Virgo is funded by the French Centre National de Recherche Scientifique (CNRS), the Italian Istituto Nazionale della Fisica Nucleare (INFN) and the Dutch Nikhef, with contributions by Polish and Hungarian institutes.

-
- [1] A. Kurkela, P. Romatschke, and A. Vuorinen. *Phys. Rev. D* **81**, 105021 (2010).
 - [2] S. Huth, P. T. H. Pang, I. Tews, et al. *Nature (London)* **606**, 276 (2022).
 - [3] B. P. Abbott et al. *Phys. Rev. Lett.* **119**, 161101 (2017).
 - [4] B. P. Abbott et al. *Phys. Rev. Lett.* **121**, 161101 (2018).
 - [5] D. Tsang, J. S. Read, T. Hinderer, A. L. Piro, and R. Bondarescu. *Phys. Rev. Lett.* **108**, 011102 (2012).
 - [6] Z. Pan, Z. W. Lyu, B. Bonga, N. Ortiz, and H. Yang. *Phys. Rev. Lett.* **125**, 201102 (2020).
 - [7] J. Zhu, C. Wang, C. Xia, E. Zhou, and Y. Ma. *Phys. Rev. D* **107**, 083023 (2023).
 - [8] J. Aasi et al. (LIGO Scientific Collaboration), *Class. Quant. Grav.* **32**, 074001 (2015).
 - [9] M. Maggiore et al. *J. Cosmol. Astropart. Phys.* **03**, 050 (2020).
 - [10] D. Reitze et al. *Bull. Am. Astron. Soc.* **51**, 035 (2019).
 - [11] K. D. Kokkotas and B. G. Schmidt, *Living Rev. Relativ.* **2**, 2 (1999).
 - [12] A. Reisenegger and P. Goldreich. *Astrophys. J.* **426**, 688 (1994).
 - [13] D. Lai. *Mon. Not. Roy. Astron. Soc.* **270**, 611 (1994).
 - [14] H. Yu and N. N. Weinberg. *Mon. Not. Roy. Astron. Soc.* **464**, 2622 (2017).
 - [15] W. C. G. Ho and D. Lai. *Mon. Not. Roy. Astron. Soc.* **308**, 153 (1999).
 - [16] W. Xu and D. Lai, *Phys. Rev. D* **96**, 083005 (2017).
 - [17] S. Y. Lau and K. Yagi. *Phys. Rev. D* **103**, 063015 (2021).
 - [18] L. Lindblom and S. L. Detweiler. *Astrophys. J. Suppl. Ser.* **53**, 73 (1983).

- [19] S. Detweiler and L. Lindblom. *Astrophys. J.* **292**, 12 (1985).
- [20] M. G. Alford, S. Han, and M. Prakash. *Phys. Rev. D* **88**, 083013 (2013).
- [21] M. G. Alford, G. F. Burgio, S. Han, G. Taranto, and D. Zappalà. *Phys. Rev. D* **92**, 083002 (2015).
- [22] Z. Y. Zhu, E. P. Zhou, and A. Li. *Astrophys. J.* **862**, 98 (2018).
- [23] C. J. Horowitz and J. Piekarewicz. *Phys. Rev. Lett.* **86**, 5647 (2001).
- [24] C. Cutler and É. É. Flanagan. *Phys. Rev. D* **49**, 2658 (1994).
- [25] S. Yoshida and Y. Eriguchi. *Astrophys. J.* **515**, 414 (1999).
- [26] H. Yu and N. N. Weinberg. *Mon. Not. Roy. Astron. Soc.* **470**, 350 (2017).
- [27] B. P. Abbott et al. *Class. Quantum Gravity* **34**, 044001 (2017).
- [28] B. P. Abbott et al. *Phys. Rev. X* **9**, 011001 (2019).
- [29] J. Buchner, A. Georgakakis, K. Nandra, et al. *Astron. Astrophys.* **564**, A125 (2014).
- [30] G. Ashton et al. *Astrophys. J. Suppl. Ser.* **241**, 27 (2019).
- [31] R. E. Kass and A. E. Raftery. *J. Am. Stat. Assoc.* **90**, 773 (1995).
- [32] Z. Q. Miao, A. Li, Z. Y. Zhu, and S. Han. *Astrophys. J.* **904**, 103 (2020).
- [33] A. Li, G. C. Yong, and Y. X. Zhang. *Phys. Rev. D* **107**, 043005 (2023).
- [34] C. J. Hogan. *Phys. Rev. Lett.* **51**, 1488 (1983).
- [35] R. G. Cai, S. He, L. Li, and Y. X. Wang. *Phys. Rev. D* **106**, L121902 (2022).
- [36] T. Fischer, N. U. F. Bastian, M. R. Wu, et al. *Nat. Astron.* **2**, 980 (2018).
- [37] K. S. Cheng and Z. G. Dai. *Phys. Rev. Lett.* **77**, 1210, (1996).
- [38] M. Q. Huber. *Physics Reports* **879**, 1 (2020).
- [39] A. Bauswein, N. U. F. Bastian, D. B. Blaschke, et al. *Phys. Rev. Lett.* **122**, 061102 (2019).
- [40] N. N. Weinberg, P. Arras, and J. Burkhart. *Astrophys. J.* **769**, 121 (2013).
- [41] C. Palenzuela, E. Barausse, M. Ponce, and L. Lehner. *Phys. Rev. D* **89**, 044024 (2014).
- [42] L. Annulli, V. Cardoso, and L. Gualtieri. *Phys. Rev. D* **99**, 044038 (2019).

Supplemental Material for “Resolving phase transition properties of dense matter through tidal-excited g-mode from inspiralling neutron stars”

A. Pulsation equations in general relativity

For the background star, the static and spherically symmetric line element is given by

$$ds^2 = g_{\mu\nu} dx^\mu dx^\nu = -e^{2\Phi} dt^2 + e^{2\lambda} dr^2 + r^2(d\theta^2 + \sin^2\theta d\phi^2) \quad (1)$$

where the metric components Φ and λ are functions of r only. We model the star as a perfect fluid, with the stress-energy-momentum tensor given by

$$T_{\mu\nu} = (p + \varepsilon)u_\mu u_\nu + pg_{\mu\nu}, \quad (2)$$

where u^μ is the four-velocity. We also assume the metric perturbation as

$$h_{\mu\nu} = -r^l H_0 e^{i\omega t} Y_{lm} dt^2 - r^l H_0 e^{i\omega t} Y_{lm} dr^2 - r^l K e^{i\omega t} Y_{lm} r^2 (d\theta^2 + \sin^2\theta d\phi^2) - 2i\omega r^{l+1} H_1 e^{i\omega t} Y_{lm} dt dr, \quad (3)$$

and the Lagrangian displacement as

$$\begin{aligned} \xi^r &= r^{l-1} e^{-\lambda} W Y_{lm} e^{i\omega t}, \\ \xi^\theta &= -r^{l-2} V \partial_\theta Y_{lm} e^{i\omega t}, \\ \xi^\phi &= -r^{l-2} \sin^{-2}\theta V \partial_\phi Y_{lm} e^{i\omega t}, \end{aligned} \quad (4)$$

where $Y_{lm}(\theta, \phi)$ is the spherical harmonics. Note the Eulerian perturbations of energy density and pressure are given by

$$\begin{aligned} \delta\varepsilon &= (p + \varepsilon)(\Delta n/n) - \xi^i \frac{d\varepsilon}{dx^i}, \\ \delta p &= \gamma p(\Delta n/n) - \xi^i \frac{dp}{dx^i}. \end{aligned} \quad (5)$$

where $\gamma = [(p + \varepsilon)/p](\partial p/\partial\varepsilon)_{\text{ad}}$ is the adiabatic index. The Lagrangian perturbation of baryon number density Δn can be derived from the baryon number conservation $\nabla_\mu(nu^\mu) = 0$, it reads

$$\Delta n = -n\nabla_i \xi^i - \frac{1}{2} n \delta g^{(3)}/g^{(3)}, \quad (6)$$

with $g^{(3)}$ the determinant of the metric of the 3-geometry at constant time. Plugging these perturbations (Eq. 3-5) into linear Einstein equation $\delta G_{\mu\nu} = 8\pi\delta T_{\mu\nu}$, one finds [1, 2]

$$\frac{dH_1}{dr} = -\left[l + 1 + \frac{2m}{r}e^{2\lambda} + 4\pi r^2(p - \varepsilon)e^{2\lambda}\right] \frac{H_1}{r} + \frac{e^{2\lambda}}{r} \left[H + K - 16(\varepsilon + p)V\right], \quad (7)$$

$$\frac{dK}{dr} = \frac{l(l+1)}{2r} H_1 + \frac{H_0}{r} - (l+1 - r\Phi') \frac{K}{r} - \frac{8\pi}{r} (\varepsilon + p)e^\lambda W, \quad (8)$$

$$\frac{dW}{dr} = -\frac{l+1}{r} W + r e^\lambda \left[\frac{1}{\gamma p} e^{-\Phi} X - \frac{l(l+1)}{r^2} V + \frac{1}{2} H_0 + K \right], \quad (9)$$

$$\begin{aligned} \frac{dX}{dr} &= -\frac{l}{r} X + (\varepsilon + p) \frac{e^\Phi}{r} \left\{ \frac{1}{2} (1 - r\Phi') H_0 + \frac{1}{2} \left(\omega^2 r^2 e^{-2\lambda} + \frac{l(l+1)}{2} \right) H_1 - \left(\frac{1}{2} - \frac{3}{2} r\Phi' \right) K - \frac{l(l+1)}{r} \Phi' V \right. \\ &\quad \left. - \left(\omega^2 e^{\lambda-2\Phi} + 4\pi(\varepsilon + p)e^\lambda - r^2 \left(\frac{1}{r^2} e^{-\lambda} \Phi' \right)' \right) W \right\}, \end{aligned} \quad (10)$$

with

$$X \equiv \omega^2(p + \varepsilon)e^{-\Phi} V - r^{-1} e^{\Phi-\lambda} p' W + \frac{1}{2}(p + \varepsilon)e^\Phi H_0. \quad (11)$$

and

$$\begin{aligned} \left(\frac{3m}{r} + \frac{(l+2)(l-1)}{2} + 4\pi r^2 p \right) H_0 &= 8\pi r^2 e^{-\Phi} X + r^2 e^{-2\lambda} \left[\omega^2 e^{-2\Phi} - \frac{l(l+1)}{2} \Phi' \right] H_1 \\ &\quad + \left[\frac{(l+2)(l-1)}{2} - \omega^2 r^2 e^{-2\Phi} + (r - 3m - 4\pi r^3 p) \Phi' \right] K. \end{aligned} \quad (12)$$

Here the prime denotes the derivative of r . We then follow the method described in Ref. [1] to solve these equations and find the eigenvalue of ω for each mode.

TABLE I: The eigenfrequency f_α and ω_α , the relativistic tidal overlap integral Q_α and the mode-mode overlap $\langle \xi_g | \xi_\alpha \rangle$ for $l = 2$ mode α . The hybrid star model is QMF+CSS with $\varepsilon_t = 250 \text{ MeV/fm}^3$ and $\Delta\varepsilon = 40 \text{ MeV/fm}^3$.

α	f_α [Hz]	$\omega_\alpha [(M/R^3)^{1/2}]$	$\langle \xi_g \xi_\alpha \rangle$	Q_α
g	574	0.0562	1	3.45e-2
f	2302	0.2254	5.18e-5	7.08e-1
p ₁	7091	0.6942	1.34e-5	1.01e-1
p ₂	11009	1.0778	-1.40e-6	4.00e-2
p ₃	14515	1.4211	-2.47e-5	-2.01e-2
$\sum_\alpha Q_\alpha^2 \approx 0.5147$				
$\langle \nabla(r^l Y_{lm}) \nabla(r^l Y_{lm}) \rangle = 0.5175$				

B. Relativistic tidal overlap integral

The orthogonal part of the Euler equation $\nabla_\mu T^{\mu\nu} = 0$ reads

$$(p + \varepsilon)u^\mu \nabla_\mu u^\nu + \perp^{\mu\nu} \nabla_\nu p = 0, \quad (13)$$

where $\perp^{\mu\nu} = g^{\mu\nu} + u^\mu u^\nu$ is the projection operator. Plugging the the Lagrangian displacement of a certain mode α , $\xi_\alpha^\mu = (0, \boldsymbol{\xi}_\alpha(r)e^{i\omega_\alpha t})$, into Eq. (13) one can derive the linear pulsation equation

$$[\mathcal{L} - (p + \varepsilon)e^{-2\Phi}\omega_\alpha^2]\xi_\alpha^\mu = 0, \quad (14)$$

with

$$\mathcal{L}\xi_\alpha^\mu = (\delta p + \delta\varepsilon)u^\nu \nabla_\nu u^\mu + \perp^{\mu\nu} \nabla_\nu \delta p + i\omega_\alpha e^{-\Phi} [(p + \varepsilon)\nabla_\nu u^\mu + u^\mu \nabla_\nu p]\xi_\alpha^\nu + i\omega_\alpha e^{-\Phi}\xi_\alpha^\mu u^\nu \nabla_\nu p. \quad (15)$$

During the inspiral, the linear perturbation of the tidal potential is governed by

$$(p + \varepsilon)u^\nu \partial_\nu \delta u^\mu + (p + \varepsilon)U^\nu \delta \Gamma_{\nu\rho}^\mu u^\rho + \mathcal{L}\xi^\mu = 0. \quad (16)$$

Plugging Eq. (14), $u^\mu = (e^{-\Phi}, 0, 0, 0)$, $\delta U^i = e^{-\Phi} \partial_t \xi^i$ and $\delta \Gamma_{00}^\mu = -1/2g^{\mu\rho} \partial_\rho h_{00}^{\text{tid}}$ into Eq. (16), one obtains

$$(p + \varepsilon)e^{-2\Phi} \frac{\partial^2}{\partial t^2} \xi^\mu + \mathcal{L}\xi^\mu = -(p + \varepsilon)e^{-2\Phi} \partial^\mu U, \quad (17)$$

where $U = -1/2h_{00}^{\text{tid}} = -M'/|\mathbf{r} - \mathbf{D}|$ is the tidal potential, D is the distance of the secondary component M' . Eq. (17) is similar to its Newtonian counterpart, see e.g., Eq.(2.5) in Ref. [3]. Therefore similar to Ref. [3], we define the relativistic tidal overlap integral as

$$Q_\alpha = \frac{\langle \xi_\alpha | \nabla(r^l Y_{lm}) \rangle}{\langle \xi_\alpha | \xi_\alpha \rangle} \quad (18)$$

where the inner product is defined as

$$\langle \xi^\mu | \psi^\mu \rangle = \int \sqrt{-g} e^{-2\Phi} (p + \varepsilon) \xi^{*\mu} \psi_\mu dx^3. \quad (19)$$

In numerical calculation, we choose the normalization $\langle \xi_\alpha | \xi_\alpha \rangle = MR^2$.

It was pointed out that the calculation of the tidal overlap integral Q_α could subject to numerical error [4, 5], thus we need to compute the eigenfunction of g-mode carefully. We check the numerical accuracy of our results in two aspects and take the Cowling approximation [6] for simplicity. First, we check the orthogonality of two modes, i.e., $\langle \xi_\alpha | \xi_{\alpha'} \rangle = MR^2 \delta_{\alpha\alpha'}$. Second, we check the sum rule $\sum_\alpha Q_\alpha^2 = \langle \nabla(r^l Y_{lm}) | \nabla(r^l Y_{lm}) \rangle$ (see e.g., in Ref [4]). We find our results satisfy the above two requirements. Table. I shows an exemplary case, where we choose the QMF+CSS model with $\varepsilon_t = 250 \text{ MeV/fm}^3$, $\Delta\varepsilon = 40 \text{ MeV/fm}^3$ and $c_s = 1$.

C. Approximations of the mode frequency and tidal overlap integral

In order to estimate the mode frequency, we consider the similar problem in Newtonian mechanics. The pulsation equation under the Cowling approximation [6] reads

$$\begin{aligned}\frac{d\xi_r}{dr} &= \left(\frac{gr}{c_{ad}^2} - 2 \right) \frac{\xi_r}{r} + \left[l(l+1) - \frac{\omega^2 r^2}{c_{ad}^2} \right] \frac{\xi_h}{r}, \\ \frac{d\xi_h}{dr} &= \left(1 - \frac{N^2}{\omega^2} \right) \frac{\xi_r}{r} + \left(\frac{N^2 r}{g} - 1 \right) \frac{\xi_h}{r},\end{aligned}\quad (20)$$

where ξ_r and ξ_h are the radial and tangential displacement, respectively. g is the gravitational acceleration. $N^2 = g^2(1/c_e^2 - 1/c_{ad}^2)$ is the Brunt-Väisälä frequency with c_e and c_{ad} the equilibrium and adiabatic sound speed, respectively. For simplicity, we assume the star is composed of two layers of incompressible fluid with $c_{ad} = c_e$, $gr/c_{ad}^2 \ll 1$ and $\omega^2 r^2/c_{ad}^2 \ll 1$. The density for the lower layer (i.e., quark core) and upper layer (i.e., hadronic envelope) are denoted as ρ^- and ρ^+ . Restrict to $l = 2$, one finds that Eq. (20) reduces to

$$\begin{aligned}\frac{d\xi_r}{dr} &= -\frac{2\xi_r}{r} + \frac{6\xi_h}{r}, \\ \frac{d\xi_h}{dr} &= \frac{\xi_r}{r} - \frac{\xi_h}{r},\end{aligned}\quad (21)$$

The general solutions can be obtained with

$$\xi_r = Ar^{-4} + Br, \quad \xi_h = -\frac{1}{3}Ar^{-4} + \frac{1}{2}Br. \quad (22)$$

Considering the regularity requirement at $r \rightarrow 0$, we obtain the solutions to Eq. (21) as

$$\xi_r = \begin{cases} r, & 0 < r < R_t, \\ \frac{\alpha R_t^4}{r^4} + \frac{\beta r}{R_t}, & R_t < r < R. \end{cases} \quad (23)$$

and

$$\xi_h = \begin{cases} \frac{1}{2}r, & 0 < r < R_t, \\ -\frac{1}{3}\frac{\alpha R_t^4}{r^4} + \frac{1}{2}\frac{\beta r}{R_t}, & R_t < r < R. \end{cases} \quad (24)$$

At the interface of two layers, ξ_r and $\Delta p = \rho g(\omega^2 r \xi_h - \xi_r)$ should be continuous, which requires

$$\begin{aligned}\alpha &= \frac{\Delta \rho}{\rho^+} \left(\frac{6}{5} \frac{M_c}{R_t^3 \omega^2} - \frac{3}{5} \right) R_t, \\ \beta &= R_t - \alpha,\end{aligned}\quad (25)$$

where $\Delta \rho \equiv \rho^- - \rho^+$ and M_c the mass of core. At the surface, the Lagrangian perturbation of the pressure must vanish, i.e., $\Delta p = 0$. Using Eq. (23-25) and replacing ρ^+ (ρ^-) with ε_t ($\varepsilon_t + \Delta \varepsilon$), we finally obtain

$$\omega^2 = \frac{(6/5)(\Delta \varepsilon/\varepsilon_t)(1-x^5) + 1 + \lambda - \sqrt{(1+\lambda)^2 - (12/5)(\Delta \varepsilon/\varepsilon_t)(\kappa-1)(1-x^5)}}{(\varepsilon_t + \Delta \varepsilon)/\varepsilon_t - (2/5)(\Delta \varepsilon/\varepsilon_t)(1-x^5)} \frac{M}{R^3}, \quad (26)$$

where $\lambda = (1/5)(\Delta \varepsilon/\varepsilon_t)[3(\kappa-1) + (3+2\kappa)x^5]$ with $x = R_t/R$ and $\kappa = (M_c/M)(R/R_t)^3$.

Previously, by analogy to the solution of the gravity waves propagated between two stratified fluid, Finn [7] pointed out that when the discontinuity near the surface (i.e., $R - R_t \ll R_t$), the frequency can be approximated as

$$\omega^2 \approx l(l+1) \frac{\Delta \varepsilon}{\varepsilon_t + \Delta \varepsilon} \frac{R - R_t}{R} \frac{M}{R^3}. \quad (27)$$

It can be seen that at the limit $x = R_t/R \rightarrow 1$, Eq. (26) reduces to the Finn's estimation Eq. (27).

TABLE II: Fitting coefficients of Eq. (30).

Model	a	b	c	d
NL3 $\omega\rho$ (stiff) +CSS	6.304	17.793	2.827	1.004
QMF (soft)+CSS	5.726	12.014	3.183	1.064

To approximate the g-mode frequencies numerically calculated in general relativity, we use the same form as Eq. (26) and Eq. (27) to fit them, namely

$$\omega^2 \approx K_1 \frac{(6/5)(\Delta\varepsilon/\varepsilon_t)(1-x^5) + 1 + \lambda - \sqrt{(1+\lambda)^2 - (12/5)(\Delta\varepsilon/\varepsilon_t)(\kappa-1)(1-x^5)}}{(\varepsilon_t + \Delta\varepsilon)/\varepsilon_t - (2/5)(\Delta\varepsilon/\varepsilon_t)(1-x^5)} \frac{M}{R^3}, \quad (28)$$

and

$$\omega^2 \approx K_2 l(l+1) \frac{\Delta\varepsilon}{\varepsilon_t + \Delta\varepsilon} \frac{R - R_t}{R} \frac{M}{R^3}. \quad (29)$$

We use the data points of stars that have $R_t > R/2$ alone to do the fitting and find the fitting factor $K_1 = K_2 = 0.015$. The results are plotted in Fig. 1. It can be seen that the estimation of Eq. (29) shows large deviations for stars with $R_t < R/2$, which is because the assumption of $R - R_t \ll R_t$ breaks down at that radius range. However, the estimation of Eq. (28) still performs well for $R_t < R/2$. The estimation errors of Eq. (28) is found to not more than $\sim 15\%$.

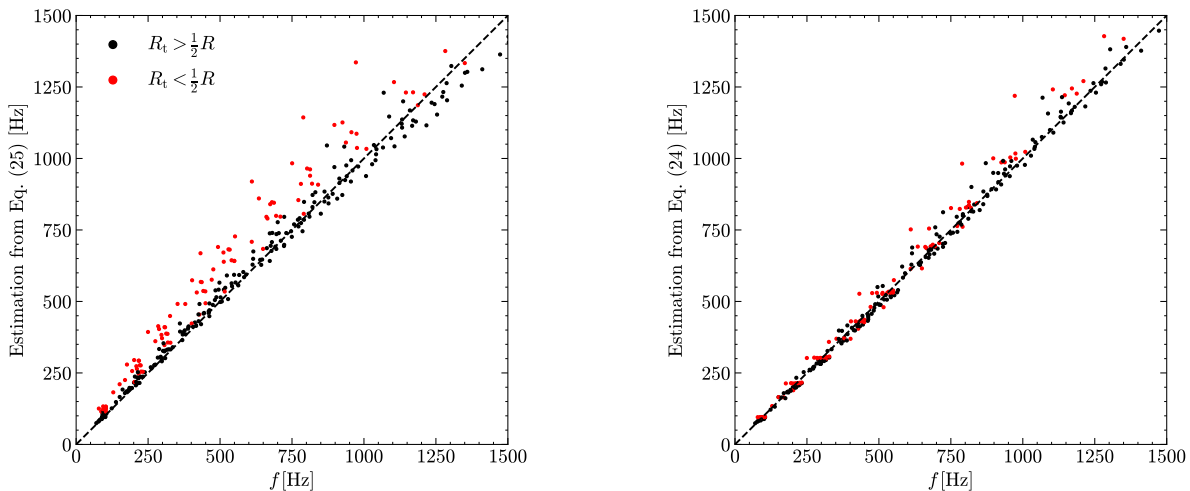


FIG. 1: Left [right] panel shows the estimated Frequencies from Eq. (29) [Eq. (28)] versus the frequencies calculated numerically from relativistic pulsation equations.

We also find a good approximation for the tidal overlap integral, as shown in Fig. 2. We should mention that such an approximation is only valid for small transition strength, i.e., $\Delta\varepsilon \lesssim 150 \text{ MeV}/\text{fm}^3$. However, higher transition strength ($\Delta\varepsilon \gtrsim 150 \text{ MeV}/\text{fm}^3$) corresponds to higher mode frequencies ($\gtrsim 1200 \text{ Hz}$) that we are not interested in, therefore we do not need to worry about them when using this approximation. By defining $\tilde{Q} \equiv Q[(\varepsilon_t + \Delta\varepsilon)(\varepsilon_t + p_t)/\varepsilon_t^2]^{-1} M_{1.4}^{-2}$, we find

$$\tilde{Q} \simeq \frac{cx(1-dx)}{e^{a(1-x)} + b}. \quad (30)$$

We fit the data points of the $1.4 M_\odot$ stars and the fitting coefficients are already listed in Table. II. It is found the estimation errors are less than $\sim 25\%$.

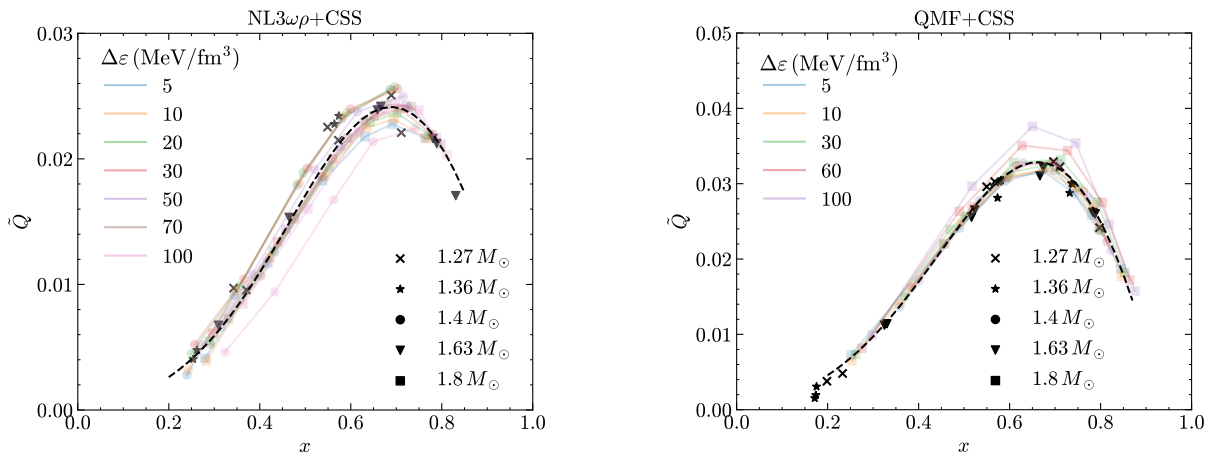


FIG. 2: Scaled tidal overlap integral \tilde{Q} versus x . The fitting lines are obtained by using data points of $1.4 M_{\odot}$ stars alone.

D. Detectability analysis

Following Ref. [8, 9], we use the Fisher information matrix to estimate the detectability of the phase shift due to resonance, assuming that the GW signal have a large signal-to-noise ratio (SNR). The Fisher information matrix for a set of parameters $\{\theta_i\}$ is defined by

$$\Gamma_{ij} = \left(\frac{\partial h}{\partial \theta_i} \middle| \frac{\partial h}{\partial \theta_j} \right), \quad (31)$$

where the inner product is defined by

$$(h_1|h_2) = 2 \int_0^{\infty} \frac{\tilde{h}_1^*(f)\tilde{h}_2(f) + \tilde{h}_1(f)\tilde{h}_2^*(f)}{S_n(f)} df, \quad (32)$$

with \tilde{h} and S_n are the Fourier transform of GW strain data and the spectral noise density of the detector. The SNR is given by $\text{SNR} = (h|h)^{1/2}$. The root-mean-square (rms) measurement error of θ_i can be written as

$$\Delta\theta_i = \sqrt{(\Gamma^{-1})_{ii}}, \quad (33)$$

where Γ^{-1} is the inverse of the Fisher information matrix. If the rms error of phase shift $\Delta|\delta\bar{\phi}|$ is smaller than $|\delta\bar{\phi}|$, then the phase shift is detectable.

We employ the IMRPhenomD_NTidal waveform [10], together with the addition of phase correction given by Eq. (5), to calculate the GW signal. The waveform parameters are

$$\{\theta_i\} = \{\mathcal{M}, q, \Lambda_1, \Lambda_2, d_L, |\delta\bar{\phi}|, \bar{f}\}. \quad (34)$$

Here for simplicity, we omit the angular dependence and the stellar rotation. We also fix the tidal deformability as $\Lambda_{1.4} = 400$ and $\Lambda_{1.8} = 300$, because it is found that $\Delta|\delta\bar{\phi}|$ is insensitive to the choice of tidal deformability. In Table. III we list some quantitative results of rms measurement errors for a $1.4 M_{\odot} - 1.4 M_{\odot}$ system.

E. Bayesian parameter estimation

We perform a Bayesian parameter estimation to analysis the GW170817 data by incorporating the resonant parameter $|\delta\bar{\phi}|$ and \bar{f} . We utilize the IMRPhenomD_NTidal waveform for the basic hypothesis \mathcal{H}_0 , whereas add the phase correction for the hypothesis \mathcal{H}_1 . The waveform parameters are given by

$$\{\theta_i\} = \{\mathcal{M}, q, \Lambda_1, \Lambda_2, \chi_{1z}, \chi_{2z}, \theta_{\text{jin}}, t_c, \phi_c, \Psi, |\delta\bar{\phi}|, \bar{f}\} \quad (35)$$

We fix the location of the source to the position determined by EM observations [11, 12] with $\alpha(J2000) = 197.45^\circ$, $\delta(J2000) = -23.38^\circ$ and $z = 0.0099$. The priors of the parameters are chosen by following those have used in Ref. [13],

TABLE III: The rms measurement errors of $|\delta\bar{\phi}|$ and \bar{f} for a $1.4 M_{\odot} - 1.4 M_{\odot}$ system.

\bar{f} (Hz)	$ \delta\bar{\phi} $	d_L (Mpc)	Detector	SNR	$\Delta\bar{f}$ (Hz)	$\Delta \delta\bar{\phi} $
500	1	100	aLIGO	49	112	0.535
			ET	502	16	0.085
			CE	1495	10	0.054
750	1	100	aLIGO	49	313	1.368
			ET	502	51	0.231
			CE	1495	32	0.148
1000	1	100	aLIGO	49	750	3.580
			ET	502	129	0.630
			CE	1495	83	0.407

except the $|\delta\bar{\phi}|$ and \bar{f} . We employ two priors for $|\delta\bar{\phi}|$ and \bar{f} , i.e., 1) Low-frequency prior with $|\delta\bar{\phi}| \sim \text{LogU}[10^{-4}, 10^2]$ and $\bar{f} \sim \text{U}[50, 400]$ Hz; 2) High-frequency prior with $|\delta\bar{\phi}| \sim \text{LogU}[10^{-4}, 10^2]$ and $\bar{f} \sim \text{U}[50, 1600]$ Hz.

In Fig. 3 we show the posterior distribution of waveform parameters. Since we use the PyMultiNest to sample from the posterior distribution, we can obtain the evidence (\mathcal{Z}) of each hypothesis directly. We then calculate their Bayes Factor with $\mathcal{B}_0^1 = \mathcal{Z}_1/\mathcal{Z}_0$. We also calculate the Bayes Factor with the Savage-Dickey Density Ratio method [15], by using the posterior distribution of hypothesis \mathcal{H}_1 alone, as

$$\frac{1}{\mathcal{B}_0^1} = \lim_{|\delta\bar{\phi}| \rightarrow 0} \frac{p(|\delta\bar{\phi}| | \text{data}, \mathcal{H}_1)}{p(|\delta\bar{\phi}| | \mathcal{H}_1)}. \quad (36)$$

Both two methods give the similar Bayes Factor, i.e., using the evidence we find $\mathcal{B}_0^1 = 0.65$ ($\mathcal{B}_0^1 = 0.72$) for low-frequency prior (high-frequency prior), whereas using the Savage-Dickey Density Ratio method we find $\mathcal{B}_0^1 = 0.78$ ($\mathcal{B}_0^1 = 1.11$) for low-frequency prior (high-frequency prior). Following the quantifying of the significance in Ref. [14], the Bayes Factor closing to unit indicates that there is no prefer for each hypothesis with current data.

-
- [1] L. Lindblom and S. L. Detweiler. *Astrophys. J. Suppl. Ser.* **53**, 73 (1983).
 - [2] S. Detweiler and L. Lindblom. *Astrophys. J.* **292**, 12 (1985).
 - [3] D. Lai. *Mon. Not. Roy. Astron. Soc.* **270**, 611 (1994).
 - [4] A. Reisenegger. *Astrophys. J.* **432**, 296 (1994).
 - [5] J. Fuller and D. Lai, *Mon. Not. Roy. Astron. Soc.* **412**, 1331 (2011).
 - [6] T. G. Cowling. *Mon. Not. Roy. Astron. Soc.* **101**, 367 (1941).
 - [7] Lee Samuel Finn. *Mon. Not. Roy. Astron. Soc.* **227**, 265 (1987).
 - [8] Curt Cutler and Éanna E. Flanagan. *Phys. Rev. D* **49**, 2658 (1994).
 - [9] Hang Yu and Nevin N. Weinberg. *Mon. Not. Roy. Astron. Soc.* **470**, 350 (2017).
 - [10] Tim Dietrich, Sebastiano Bernuzzi, and Wolfgang Tichy. *Phys. Rev. D* **96**, 121501 (2017).
 - [11] B. P. Abbott et al. *Astrophys. J. Lett.* **848**, L12 (2017).
 - [12] A. J. Levan, J. D. Lyman, N. R. Tanvir, et al. *Astrophys. J. Lett.* **848**, L28 (2017).
 - [13] B. P. Abbott et al. *Phys. Rev. X* **9**, 011001 (2019).
 - [14] R. E. Kass and A. E. Raftery. *J. Am. Stat. Assoc.* **90**, 773 (1995).
 - [15] J. M. Dickey and B. P. Lientz. *Ann. Math. Statist.* **41**, 214 (2019).

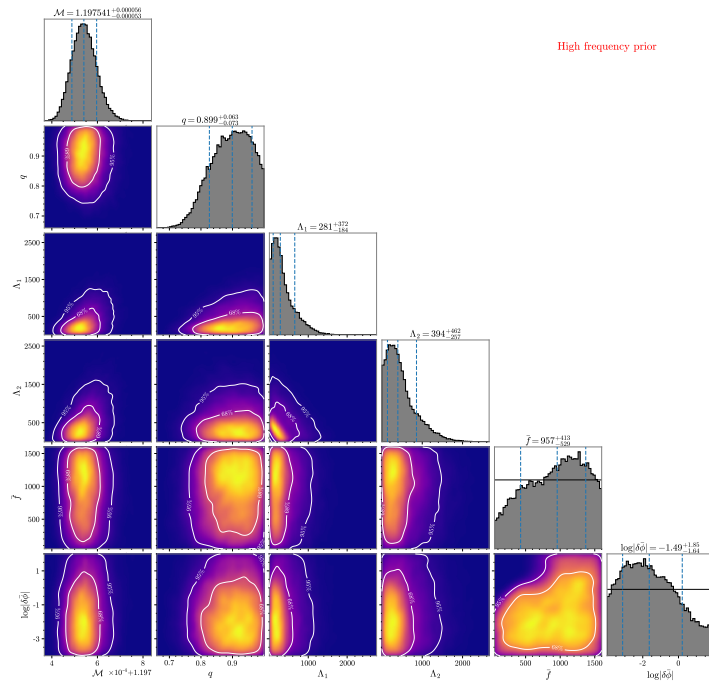
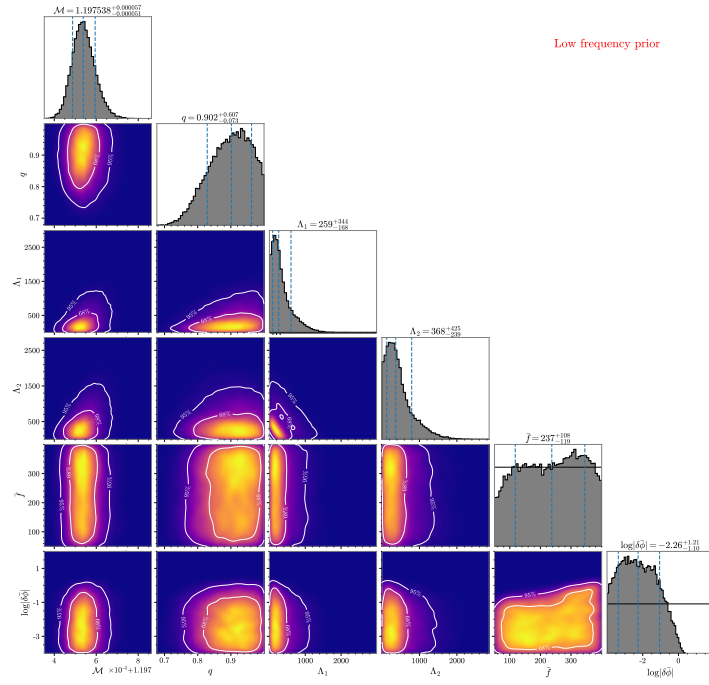


FIG. 3: The posterior distributions of the parameters for low-frequency prior (upper) and high-frequency prior (lower). The horizontal line in last two diagonal panels denote the prior distributions of corresponding parameters.